Current Measurement Errors Compensation Based on Current Ripple Component Decoupling for PMSM Drives

Hanbing Dan, *Senior Member, IEEE,* Huaibin Pang, Yonglu Liu, *Member, IEEE,* Yao Sun, *Member, IEEE,* and Mei Su, *Member, IEEE*

***Abstract*—Current measurement errors (CME) including offset error and scaling error exist in permanent magnet synchronous motor (PMSM) drive systems. It will cause periodic ripples in the *dq*-axis currents and motor torque/speed. Thus, this paper proposes a novel method to decouple and compensate for the current measurement errors based on the *d*-axis current ripple component. In the proposed method, the separation of CME from the measured current takes into account the influence of the closed-loop system. The adaptive band-pass filter is employed to extract the desired periodic ripple component in the *d*-axis current. Decoupling of the CME is achieved through a simple mathematical operation and a low-pass filter. Compensation is performed through the integrator operation. The proposed method effectively eliminates the *dq*-axis current ripple and speed ripple caused by the CME. The proposed method has robustness performance on motor parameters and can be used during the operation of the motor. The effectiveness and practicability of the proposed CME compensation method is verified by the experimental results.**

***Index Terms*—Current measurement error, permanent magnet synchronous motor, speed ripple.**

I. Introduction

THE accurate measurement of stator current is crucial in the permanent magnet synchronous motor (PMSM) vector control system [1]. Current measurement errors (CME) are inevitable in PMSM drives due to non-linear components, imbalances in sensor power supply, and thermal drift in the current measurement circuit [2]. The CME manifest as offset error and scaling error in the measurement of stator current, resulting in first- and second-order speed ripples [3]. The presence of speed ripples negatively impacts the performance of motor drives and can lead to damage or fatigue of mechanical components in severe cases [4]. Consequently, it is necessary to develop compensation algorithms for CME in high-performance motor control systems. Extensive research has explored various compensation schemes for CME, which can be categorized as offline compensation [5–7] and online compensation [8–23].

Offline compensation refers to the process of calibrating the current measurement sensor. During the initial commissioning, the offset error can be calibrated offline [5]. Some proposed offline methods aim to compensate for both offset error and scale error [6], [7], but they do not fully address the issue that the error might change due to thermal drift during operation.

Online compensation methods can be further categorized into two types: those based on other measurable information in the drive system [8–17] and those based on the current information itself [18–23]. Methods such as the resonant controller [8], iterative learning control [9], and repetitive control [10] directly eliminate periodic speed/torque ripples. Although effective for tackling speed/torque ripples, these methods do not provide direct compensation for CME itself. In scenarios demanding high-precision stator current, such as sensorless control, CME still require compensation. In [11], [12], and [13], proportional integral (PI) observer, model-based observer, and adaptive extended state observer are used to estimate CME, respectively. These proposed methods treat CME as a disturbance in the *dq*-axis currents and employ the idea of disturbance-observer-based control to eliminate it [14]. However, the observer has parameter sensitivity, which increases the design complexity. The voltage reference signal produced by the current controller is also utilized to compensate for CME [15], [16]. In [15], the proposed algorithm divides the output signal of the *d*-axis PI current regulator into six segments for each electrical cycle to calculate the compensation for CME. In [16], the CME is obtained using either the positive or negative sequence component of the voltage error. However, these methods are constrained by the performance of the PI current regulator and can lead to transient performance degradation. In [17], a method is proposed to compensate for CME by artificially injecting multiple instances of current errors and extracting speed harmonic information for CME calculation. However, this method requires stable motor operation, and the current and speed ripples can be aggravated during the error-injecting process.

On the other hand, the extraction and compensation of CME directly from the current signal are commonly practiced. For example, a discrete Fourier transform (DFT) based phase discrimination approach can be used to separate ripple signals from the current [18]. However, DFT calculations can be computationally complex. Recursive sliding window least-square (RSWLS) method [19] is utilized for online compensation. However, this method is reliant on accurate motor parameters and solely addresses scaling errors. Additionally, in [20] and [21], ripple extraction algorithms using machine learning and artificial intelligence have been suggested. Nevertheless, the implementation of artificial intelligence algorithms on cheap microcontrollers is currently intricate. In [22], a compensation technique involving the filtering of the discrepancy between the predicted and measured currents has been proposed. However, the accuracy of current prediction hinges on the precise

motor parameters. An adaptive-frequency harmonic suppression strategy based on vector reconstruction is proposed in [23]. This method can decouple the fundamental component frequency from the harmonics in the current vector. However, the compensation performance of this method depends on the performance of the harmonic suppressor.

This paper proposes a novel CME compensation method based on decoupling the current ripple component to achieve simple, efficient, and robust compensation. An adaptive band-pass filter is utilized to extract the periodic ripple component in the *d*-axis current. The extracted signal is manipulated by specific trigonometric functions and then filtered through a low-pass filter to isolate the CME decoupling value. The compensation is executed through integrator operation. The method is implemented without requiring additional devices and has robustness performance on motor parameters.

The subsequent sections of this paper are structured as follows: Section II presents an analysis of the CME. Section III scrutinizes the response of CME within the closed-loop system and introduces the CME estimation and compensation method. The experimental findings are outlined in Section IV. Section V offers a conclusion to the paper.

II. Analysis of Current Measurement Errors

Stator currents are commonly measured using current sensors, which are then processed through a low-pass filter to suppress switching noise, and finally converted with A/D converters [15]. Various factors, including power supply voltage imbalances in the current sensor and the presence of analog devices in the current measurement path, result in offset error [24].

Scaling error is another type of CME. In order for the analog-to-digital converter to operate effectively, the output of the current sensor must be adjusted to fit within its input range. Additionally, the current controller needs to convert this digital signal into the true value of the current [25]. During this conversion process, adjustments to the signal ratio are necessary, which can lead to the occurrence of scaling errors.

The measured three phase current with the CME can be expressed as:

$$\begin{cases} i_{a\_s} = K_a i_a + \Delta i_a \\ i_{b\_s} = K_b i_b + \Delta i_b \\ i_{c\_s} = -i_{a\_s} - i_{b\_s} \end{cases} \tag{1}$$

where i_a and i_b are the actual stator currents. i_{a_s}, i_{b_s} and i_{c_s} are the measured three-phase stator currents, Δi_a and Δi_b are the offset values and K_a and K_b represent the scaling factors of phase A current and phase B current respectively.

Due to the high performance of current control, it can be assumed that the measured currents exactly follow their reference values. The constraint equation is as follows:

$$\begin{bmatrix} i_{d\_s} \\ i_{q\_s} \end{bmatrix} = \begin{bmatrix} i_d^* \\ i_q^* \end{bmatrix} = \frac{2}{3} T_{2s/2r} T_{3/2} \begin{bmatrix} i_{a\_s} \\ i_{b\_s} \\ i_{c\_s} \end{bmatrix} \tag{2}$$

where i_{d_s} and i_{q_s} are the measurement currents in the synchronous reference frame (dq-frame/SRF), i_d^* and i_q^* are reference currents in the SRF, and

$$T_{2s/2r} = \begin{bmatrix} \cos\theta_e & \sin\theta_e \\ -\sin\theta_e & \cos\theta_e \end{bmatrix}$$

$$T_{3/2} = \begin{bmatrix} 1 & -\frac{1}{2} & -\frac{1}{2} \\ 0 & \frac{\sqrt{3}}{2} & -\frac{\sqrt{3}}{2} \end{bmatrix}$$

By substituting (1) into (2), the value of the actual currents i_a and i_b can be obtained. And actual currents in the SRF are as follows:

$$\begin{bmatrix} i_d \\ i_q \end{bmatrix} = \frac{2}{3} T_{2s/2r} T_{3/2} \begin{bmatrix} i_a \\ i_b \\ -i_a - i_b \end{bmatrix} \tag{3}$$

The *dq*-axis error currents are solved by:

$$\begin{bmatrix} \Delta i_d \\ \Delta i_q \end{bmatrix} = \begin{bmatrix} i_{d\_s} - i_d \\ i_{q\_s} - i_q \end{bmatrix} \tag{4}$$

Offset error and scaling error are independent of each other and can be discussed separately.

The error current that demonstrates only an offset error occurs when setting $K_a = K_b = 1$. The offset errors are represented as follows:

$$\begin{cases} \Delta i_{d\_off} = \Delta i_a \cos\theta_e + \dfrac{1}{\sqrt{3}}(2\Delta i_b + \Delta i_a)\sin\theta_e \\ \Delta i_{q\_off} = -\Delta i_a \sin\theta_e + \dfrac{1}{\sqrt{3}}(2\Delta i_b + \Delta i_a)\cos\theta_e \end{cases} \tag{5}$$

From (5), the offset error Δi_{dq_off} are solely associated with Δi_a and Δi_b, consequently making it an independent variable. The offset error induces the presence of the first-order harmonic.

Assuming only scaling error exists by setting $\Delta i_a = \Delta i_b = 0$, the scaling error are shown as:

$$\begin{bmatrix} \Delta i_{d\_scale} \\ \Delta i_{d\_scale} \end{bmatrix} = H \begin{bmatrix} i_d^* \\ i_q^* \end{bmatrix} \tag{6}$$

where H is shown below.

It can be seen from (6) that the scaling error is affected by two factors: the reference current and the scaling coefficient K_a and K_b. The scaling error primarily resulting in the second-order harmonic.

$$H = \begin{bmatrix} -\frac{3(K_b+K_a)+(K_b-K_a)2\sqrt{3}\sin\left(2\theta+\frac{\pi}{3}\right)-6K_aK_b}{6K_aK_b} & -\frac{(K_a-K_b)(\sqrt{3}-\sqrt{3}\cos(2\theta)+3\sin(2\theta))}{6K_aK_b} \\ -\frac{(K_a-K_b)(3\sin(2\theta)-\sqrt{3}(1+\cos(2\theta))}{6K_aK_b} & -\frac{3(K_a+K_b)+(K_a-K_b)2\sqrt{3}\sin\left(2\theta+\frac{\pi}{3}\right)-6K_aK_b}{6K_aK_b} \end{bmatrix}$$

III. Analysis and Design for Proposed CME Compensation Method

From (5) and (6), the estimation of offset and scaling errors can be achieved by separating the ripple component. However, the ripple component is affected by the closed-loop system. Therefore, it is necessary to establish a model for the closed-loop system on the CME initially. Since the offset error is treated as an independent variable, while the scaling error is not independent, separate models should be established for them.

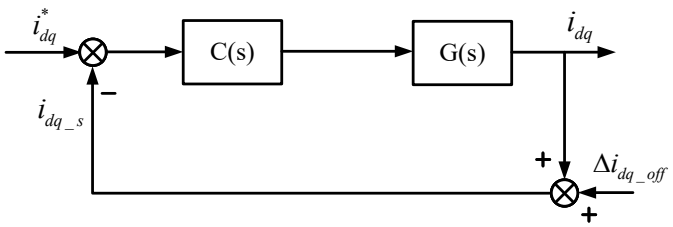

Fig. 1. General block diagram of the current control system with offset error.

A. Offset Error

The complex vector form voltage equation of PMSM in the SRF is:

$$u_{dq} = R_s i_{dq} + L_s p i_{dq} + j\omega_e i_{dq} + e_{dq} \tag{7}$$

where $u_{dq} = u_d + ju_q$ and $i_{dq} = i_d + ji_q$ are the complex vector voltage and current, $e_{dq} = e_d + je_q = j\omega_e\psi_f$ is the complex vector back electromotive force (EMF), R_s is the stator resistance, L_s is the stator inductance, ω_e is the electrical frequency, p is the differential operator and ψ_f is the permanent magnetic flux.

Under the assumption that ω_e remains constant throughout a single control interval, the transfer function of the voltage model can be derived as:

$$\begin{aligned} i_{dq}(s) &= \frac{1}{R_s + sL_s + j\omega_e L_s}(u_{dq}(s) - e_{dq}(s)) \\ &\triangleq G(s)(u_{dq}(s) - e_{dq}(s)) \end{aligned} \tag{8}$$

Assuming that back EMF compensation is complete, a general block diagram of the current control system with offset error is shown in Fig. 1. Within the diagram, $C(s)$ is the current controller. For the complex vector PI controller [26], $C = K_p(1 + (K_i + j\omega_c)/s)$, $K_p = \omega_c L_s$, $K_i = R_s/L_s$, and ω_c is the current loop bandwidth. i^*_{dq}, i_{dq_s} and Δi_{dq_off} represent the reference current, measurement current, and offset error in the complex vector, respectively.

Since the CME changes slowly, the Δi_{dq_off} is assumed to be constant. The transfer function of the current loop is as follows:

$$i_{dq} \triangleq G_{yr}(s) i^*_{dq} + G_{yn}(s)\Delta i_{dq\_off} \tag{9}$$

where

$$\begin{cases} G_{yr}(s) = \dfrac{GC}{1+GC} = \dfrac{\omega_c}{s+\omega_c} \\ G_{yn}(s) = \dfrac{-GC}{1+GC} = -\dfrac{\omega_c}{s+\omega_c} \end{cases} \tag{10}$$

$G_{yr}(s)$ and $G_{yn}(s)$ represent the response of the actual current to the reference current and measurement error respectively.

By substituting (4) to (9), the transfer function of the measurement current is shown as:

$$i_{dq\_s} = G_{yr}(s) i^*_{dq} + G_{yn}(s)\Delta i_{dq\_off} + \Delta i_{dq\_off} \tag{11}$$

By subtracting the reference value and introducing the $G_e(s) \triangleq 1 + GC = (s + \omega_c)/\mathrm{s}$, the Δi_{dq_off} can be obtained:

$$\Delta i_{dq\_off} = G_e(s)(i_{dq\_s} - G_{yr}(s) * i^*_{dq}) \tag{12}$$

In general PMSM vector control systems, the *d*-axis typically operates without an outer-loop, while the *q*-axis generally incorporates a speed outer loop. As a result, i^*_d remains constant, whereas i^*_q may vary. Furthermore, the *d*-axis is not influenced by the performance of back EMF compensation. Consequently, the *d*-axis current is selected as the target for decoupling the ripple component.

Once the ripple current is calculated by (12), it is subsequently filtered through an adaptive band-pass filter (BPF) with a resonant frequency of ω_e. The CME consequently result in first- and second-order harmonics. Harmonics can also arise from periodic load torque variations and other potential sources. To reduce interference from other harmonics and avoid the integral saturation effect induced by $G_e(s)$. The center resonant frequency of the adaptive BPF can vary with changes in the fundamental frequency of the motor. The transfer function of the BPF is defined as:

$$G_{BPF\_1}(s) = \frac{2k_{r1}\omega_{c1}s}{s^2 + 2\omega_{c1}s + \omega_e^2} \tag{13}$$

where k_{r1} is the gain coefficient and ω_{c1} is the bandwidth of the filter. They are set as $k_{r1} = 1, \omega_{c1} = 5$ to ensure a reasonable frequency selection range and a gain of 1 at the resonant frequency.

Then, Δi_{d_off} in (5) is multiplied by a trigonometric function factor $\cos(\theta_e)$ as (14).

Subsequently, it is fed into a low-pass filter (LPF). The output of the LPF is shown as:

$$\mathrm{LPF}\left\{\cos\theta_e \cdot \Delta i_{d\_off}\right\} \approx \frac{1}{4}\Delta i_a \tag{15}$$

$$\cos\theta_e \cdot \Delta i_{d\_off} = \frac{1}{4}\Delta i_a + \frac{1}{4}\Delta i_a \cos 2\theta_e + \frac{1}{2\sqrt{3}}(2\Delta i_b + \Delta i_a)\sin 2\theta_e \tag{14}$$

$$-\cos(\theta_e + \frac{\pi}{3}) \cdot \Delta i_{d\_off} = \frac{1}{2}\Delta i_b + \frac{1}{2}\Delta i_a \cos 2\theta_e + \frac{\sqrt{3}}{6}\sin 2\theta_e - \frac{1}{2\sqrt{3}}\Delta i_b \sin 2\theta_e - \frac{1}{2}\Delta i_b \cos 2\theta_e \tag{16}$$

Similarly, Δi_{d_off} is multiplied by another trigonometric function factor $-\cos(\theta_e + \pi/3)$ as (16). The output of the LPF is:

$$\mathrm{LPF}\left\{-\cos(\theta_e + \frac{\pi}{3}) \cdot \Delta i_{d\_off}\right\} \approx \frac{1}{2}\Delta i_b \tag{17}$$

From (15) and (17), the offset error can be estimated. To ensure smooth and precise compensation, an integral controller is employed to force the output of the LPF to zero. The outputs of the integrator, $\Delta\hat{i}_a$ and $\Delta\hat{i}_b$, serve as compensation of the offset errors in the phase A and phase B current measurements, respectively. The block diagram of the offset error compensation structure is illustrated in Fig. 3.

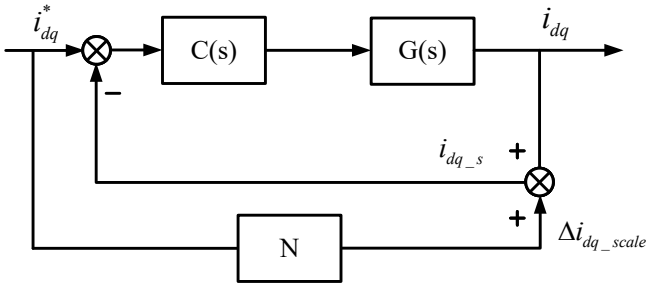

Fig. 2. General block diagram of the current control system with scaling error

B. Scaling Error

By applying the Laplace transform to (6), the following expression in complex vector form can be derived as:

$$\Delta i_{dq\_scale} = N(s) i^*_{dq} \tag{18}$$

where $N(s)$ represents the Laplace transform of H.

The general block diagram of the current control system with scaling error is shown in Fig. 2. The transfer function of the current loop is as follows:

$$i_{dq} = \frac{GC(1-N)}{1+GC} i^*_{dq} \tag{19}$$

The measurement current is shown as:

$$\begin{aligned} i_{dq\_s} &= i_{dq} + \Delta i_{dq\_scale} \\ &= \frac{CG}{1+CG} i^*_{dq} + \frac{1}{1+CG} N i^*_{dq} \end{aligned} \tag{20}$$

It can be observed that (20) has a similar form to (11). By subtracting the reference value and introducing the $G_e(s)$, the Δi_{dq_scale} can be obtained:

$$\Delta i_{dq\_scale} = G_e(s)(i_{dq\_s} - \frac{\omega_c}{s+\omega_c} i^*_{dq}) \tag{21}$$

The adaptive BPF with a resonant frequency of $2\omega_e$ is implemented to minimize the impact of harmonic components other than the second harmonic:

$$G_{BPF\_2}(s) = \frac{2k_{r2}\omega_{c2}s}{s^2 + 2\omega_{c2}s + 4\omega_e^2} \tag{22}$$

The parameters of BPF2 are identical to those of BPF1. Similar to BPF1, the center frequency of BPF2 can vary with changes in the fundamental frequency of the motor.

The output of the BPF in real vector form undergoes the inverse Laplace transform, resulting in the following expression:

$$BPF\{\begin{bmatrix} \Delta i_{d\_scale} \\ \Delta i_{q\_scale} \end{bmatrix}\} = R \begin{bmatrix} i^*_{d\_\sec} \\ i^*_{d\_dc} \\ i^*_{q\_\sec} \\ i^*_{q\_dc} \end{bmatrix} \tag{23}$$

where $i^*_{d\_\sec}$ and $i^*_{q\_\sec}$ are second harmonic components in *dq*-axis current reference, $i^*_{d\_dc}$ and $i^*_{q\_dc}$ are the DC components in *dq*-axis current reference and R is a 2×4 order matrix of H as indicated below.

Then, by multiplying a trigonometric function factor $\cos(2\theta_e + \pi/3)$ to (23), it can be obtained:

$$\cos(2\theta + \frac{\pi}{3}) \cdot BPF\{\begin{bmatrix} \Delta i_{d\_scale} \\ \Delta i_{q\_scale} \end{bmatrix}\} = M \begin{bmatrix} i^*_{d\_\sec} \\ i^*_{d\_dc} \\ i^*_{q\_\sec} \\ i^*_{q\_dc} \end{bmatrix} \tag{24}$$

where $M = \cos(2\theta + \frac{\pi}{3}) \cdot R$ is shown below.

It can be seen from (24) that it consists of both DC components and harmonic components. This implies that the parameters K_a and K_b can be extracted from the DC component. The following is a qualitative analysis of its constituents.

Because the *d*-axis current loop operates without an outer loop and the reference current i^*_d remains constant, the $i^*_{d\_\sec}$ becomes zero. The response of the first column of matrix M can be disregarded.

$i^*_{d\_dc}$ generates the second harmonic on the *d*-axis, while it produces both the DC component and the second harmonic on the *q*-axis. However, considering that $i^*_d = 0$ type vector

$$R = \begin{bmatrix} -\frac{3(K_a+K_b)-6K_aK_b}{6K_aK_b} & -\frac{2\sqrt{3}(K_b-K_a)\sin\left(2\theta+\frac{\pi}{3}\right)}{6K_aK_b} & -\frac{\sqrt{3}(K_a-K_b)}{6K_aK_b} & -\frac{(K_a-K_b)(3\sin(2\theta)-\sqrt{3}\cos(2\theta))}{6K_aK_b} \\ \frac{\sqrt{3}(K_a-K_b)}{6K_aK_b} & -\frac{(K_a-K_b)(3\sin(2\theta)-\sqrt{3}\cos(2\theta))}{6K_aK_b} & -\frac{3(K_a+K_b)-6K_aK_b}{6K_aK_b} & -\frac{2\sqrt{3}(K_a-K_b)\sin\left(2\theta+\frac{\pi}{3}\right)}{6K_aK_b} \end{bmatrix}$$

$$M = \begin{bmatrix} (1-\frac{K_a+K_b}{2K_aK_b})\cos(2\theta+\frac{\pi}{3}) & \frac{\sqrt{3}\sin(4\theta+\frac{2\pi}{3})(K_a-K_b)}{6K_aK_b} & \frac{\sqrt{3}(K_b-K_a)\cos(2\theta+\frac{\pi}{3})}{6K_aK_b} & \frac{\sqrt{3}(K_a-K_b)\left(1+\cos(2\theta+\frac{\pi}{3})\right)}{6K_aK_b} \\ \frac{\sqrt{3}(K_a-K_b)\cos(2\theta+\frac{\pi}{3})}{6K_aK_b} & \frac{\sqrt{3}(K_a-K_b)\left(1+\cos(2\theta+\frac{\pi}{3})\right)}{6K_aK_b} & (1-\frac{K_a+K_b}{2K_aK_b})\cos(2\theta+\frac{\pi}{3}) & \frac{\sqrt{3}\sin(4\theta+\frac{2\pi}{3})(K_b-K_a)}{6K_aK_b} \end{bmatrix}$$

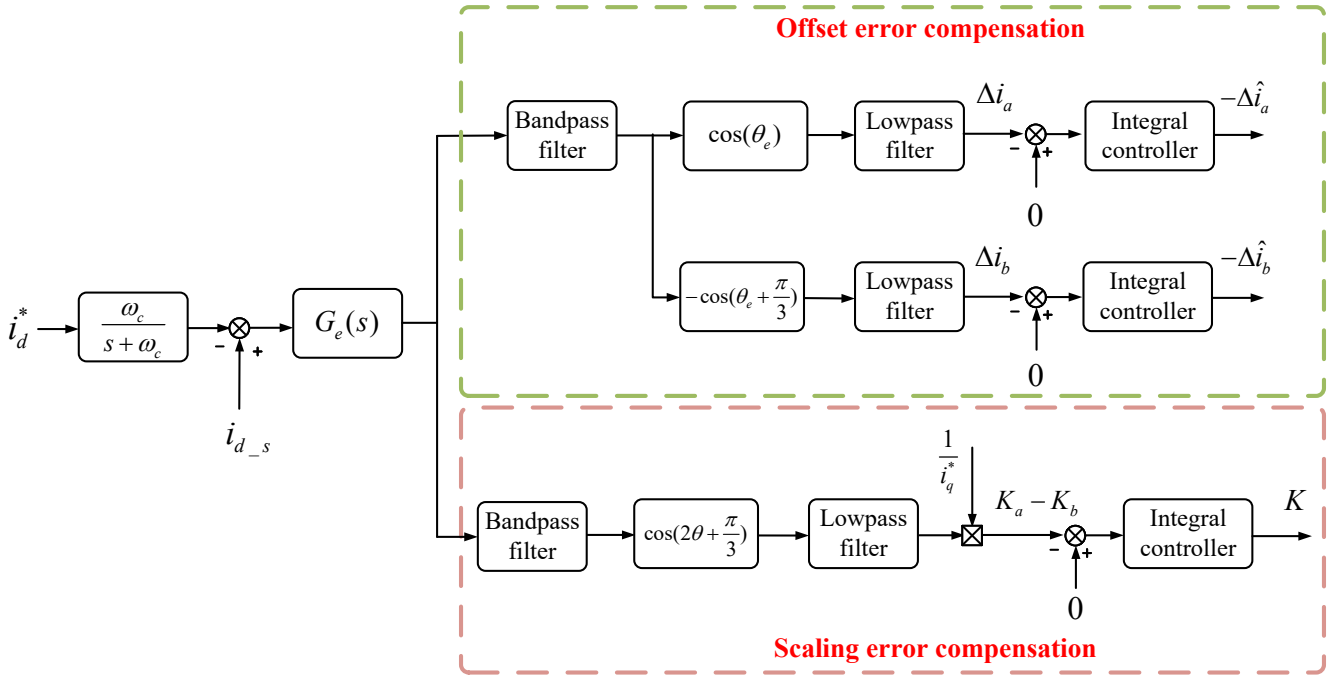

Fig. 3. General block diagram of proposed CME compensation method

control is commonly employed, this DC component is not suitable for decoupling K_a and K_b.

The transfer function from the CME to the speed error is [3]:

$$\Delta\omega_e = -\frac{K_T W}{1 + C_s W}\Delta i_q \tag{25}$$

where K_T is torque constant, $C_s = K_{ps} + K_{is}/s$ is speed controller, K_{ps} and K_{is} are the proportional and integral gain of the speed controller, $W = 1/(Js + B)$ is motor motion plant, J is moment of inertia, and B is viscous friction.

The transfer function from the speed error to the current reference is:

$$i_q^* = C_s \Delta\omega_e \tag{26}$$

By substituting (25) into (26), the transfer function from the CME to the current reference is:

$$i_q^* = -\frac{K_T C_s W}{1 + C_s W}\Delta i_q \triangleq E(s)\Delta i_q \tag{27}$$

Since $E(s)$ acts as a low-pass unit, the response of $i_{q\_\sec}^*$ can be ignored.

$i_{q\_dc}^*$ generates the DC component and the second harmonic on the d-axis, while it creates the second harmonic on the q-axis. Therefore, the target for decoupling the K_a and K_b is selected as the d-axis.

Subsequently, it is passed through a LPF to extract the DC component, with the output of the LPF given by:

$$\mathrm{LPF}\left\{\cos(2\theta_e + \frac{\pi}{3}) \cdot \mathrm{BPF}\left\{\Delta i_{d\_scale}\right\}\right\} \approx \frac{\sqrt{3}(K_a - K_b) i_{q\_dc}^*}{6(K_a K_b)} \tag{28}$$

The direction of $i_{q\_dc}^*$ aligns with the direction of i_q^*. To ensure that the direction of the compensation value is

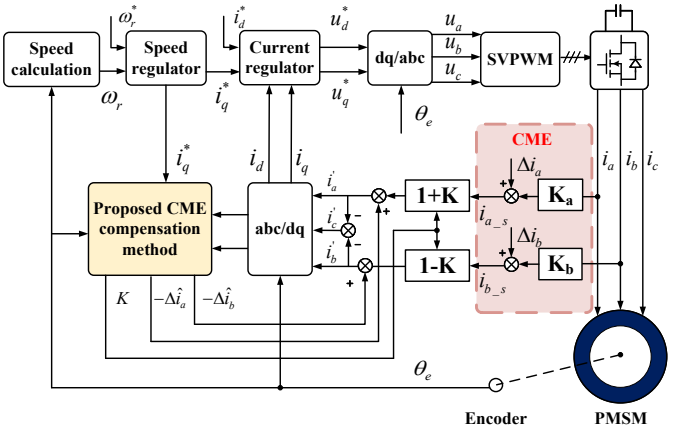

Fig. 4. The vector control scheme with proposed CME compensation structure

exclusively influenced by $K_a - K_b$, the LPF output can be divided by i_q^*.

Then, it is regulated to 0 by means of an integral controller. The output of the integral controller represents the scaling error compensation coefficient K. The block diagram of the scaling error compensation method is illustrated in Fig. 3.

K shows an inverse proportionality to $K_a - K_b$. The measurement current of phase A is multiplied by $(1 + K)$, and the measurement current of phase B is multiplied by $(1 - K)$. The currents after compensating for the scaling error are shown as:

$$\begin{cases} i_{a\_com} = K_a(1 + K) i_a = K_a^c i_a \\ i_{b\_com} = K_b(1 - K) i_b = K_b^c i_b \end{cases} \tag{29}$$

where K_a^c and K_b^c are the compensated scaling factors.

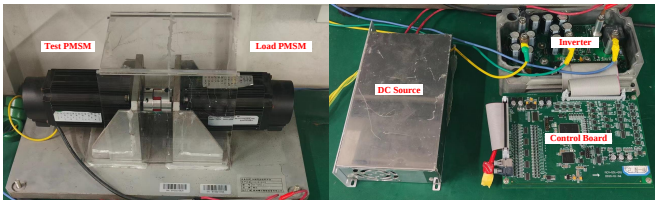

Fig. 5. Experimental setup

If $K_a - K_b > 0$, then $K < 0$, $(1-K) > 1$,$(1+K) < 1$. Then K_a^c decreases, and K_b^c increases relatively. Then $(K_a^c - K_b^c)$ decreases and gradually approaches 0.

If $K_a - K_b < 0$, then $K > 0$, $(1-K) < 1$,$(1+K) > 1$. Then K_a^c increases, and K_b^c decreases relatively. Then $(K_a^c - K_b^c)$ increases and gradually approaches to 0.

Finally, the scaling measurement error is corrected.

The vector control scheme with proposed CME compensation structure is shown in Fig. 4.

IV. Experimental Results

The experimental setup as shown in Fig. 5 is carried out on the PMSM drive with a TI TMS320F28335 digital signal processor (DSP). The parameters of the PMSM are shown in Table I.

Two uncorrected current sensors are used to sample the A-phase and B-phase currents. The current value is calculated by the sampling coefficient as follows:

$$\begin{aligned} I_{a\_s} &= K_{sample\_a}(D_a - D_{sample\_a}) \\ I_{b\_s} &= K_{sample\_b}(D_b - D_{sample\_b}) \end{aligned} \tag{30}$$

where K_{sample_a} and K_{sample_b} are the scaling factors, D_{sample_a} and D_{sample_b} are the offset factors, D_a and D_b are the current measurement digital signal in decimal.

Although the CME occur during the sampling process, it manifests as the discrepancy between the sampling coefficient used in the DSP and the actual sampling coefficient. The specific sampling coefficients used in the experiments are provided in Table II.

TABLE I
Parameters of The PMSM

Parameter	Value
Rated power	0.2 kW
Rated voltage	14 V
Rated current	10 A
Pole pairs	5
Stator resistance	0.017 Ω
Stator inductance	0.29 mH
Rated torque	5 N·m

TABLE II
Sampling Coefficient

Quantity	K_{sample_a}	K_{sample_b}	D_{sample_a}	D_{sample_b}
Actual value	0.0184	0.0495	2043	2044
Test value	0.0123	0.0593	2034	2068

As described in (30), the offset error arises due to a combination of scaling and offset coefficients. The use of uncalibrated or miscalibrated sensors provides a more realistic approach than injecting inherent scaling errors and offset errors separately.

A. Performance of Proposed CME Compensation Method in Steady-State Conditions

The experimental waveforms of speed, *dq*-axis currents, the first- and second-oreder harmonic currents extracted through BPF1 and BPF2, compensation amount $\Delta\hat{i}_a$, $\Delta\hat{i}_b$ and K at 240 r/min using the proposed CME compensation method are shown in Fig. 6. In Fig. 6(a), (b), and (c), the speed ripples and *dq*-axis currents ripples decrease steadily during the compensation process. As shown in Fig. 6(d) and (e), the first- and second-oreder harmonic currents in *d*-axis current are greatly eliminated. Fig. 6(f) shows the stable convergence of the compensation amount.

The contrast of the harmonic content in steady-state *q*-axis current with and without compensation is shown in Fig. 7. It can be observed from Fig. 7(a) that the major components are the first- and second-order harmonics, which account for 5.48% and 8.58% respectively. The lower frequency harmonics are mechanical frequency harmonics caused by slight shaft misalignment and have no impact on this experiment [27]. The FFT analysis results with compensation show that the first- and second-order harmonic components decrease to 0.41% and 1.03% as shown in Fig. 7(b).

The comparison of the motor phase currents with and without compensation is shown in Fig. 8. From Fig. 8(a), it can be observed that the currents of phase A and phase B are asymmetrical without compensation, ranging from –3.2A to 4A and from –4A to 2.4A, respectively. With compensation, the asymmetry in the motor phase currents caused by CME has been effectively eliminated and almost completely disappears as shown in Fig. 8(b).

B. Performance of Proposed CME Compensation Method in Dynamic Conditions

The performance of the proposed compensation method is tested in dynamic conditions in Fig. 9. As shown in Fig. 9(a) and (b), the motor command speed is set from 240 r/min to 360 r/min to 120 r/min subsequently. It can be seen that the proposed CME compensation method has no impact on the dynamic performance of the motor drive system, and the compensation is effective in all speed segments. As shown in Fig. 9(c) and (d), the motor undergoes loading and unloading. The performance of the proposed CME compensation method is unaffected by the load variations and has a high robustness against the load disturbances.

Fig. 9 shows that the dynamic performance of the PMSM drive system with the proposed CME compensation method closely resembles the dynamic performance of the PMSM in normal state. Consequently, the adoption of the proposed method does not impact the dynamic control performance. Furthermore, the steady-state speed error has been improved across various working conditions.

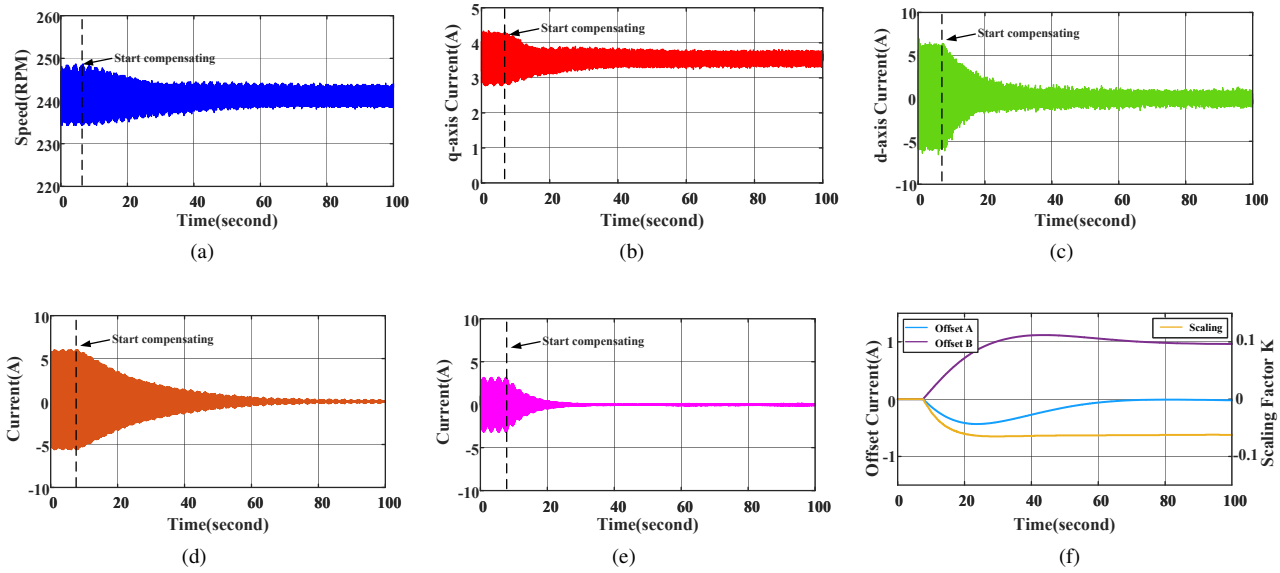

Fig. 6. Performance of vector control scheme with proposed CME compensation method at 240rpm. (a) Speed. (b) i_q. (c) i_d. (d) BPF1 current. (e) BPF2 current. (f) Compensation value.

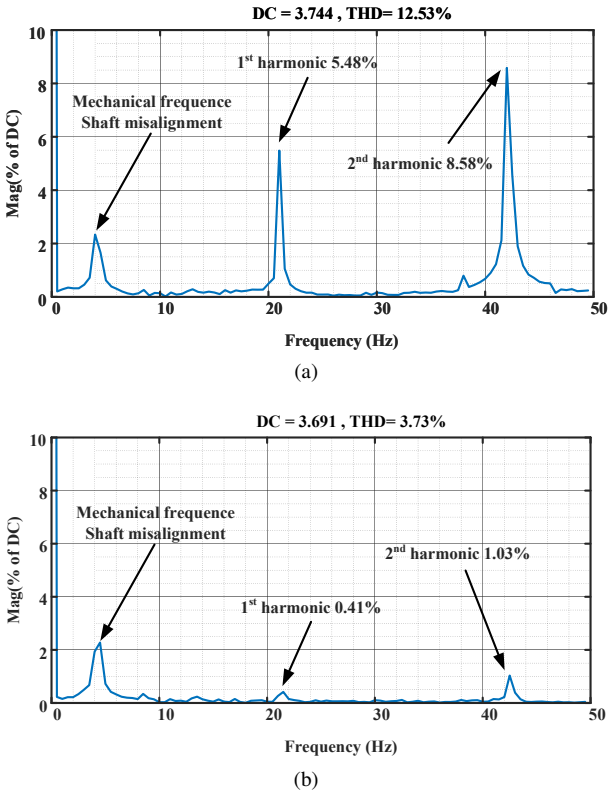

Fig. 7. FFT analysis for q-axis current. (a) Without compensation. (b) With compensation.

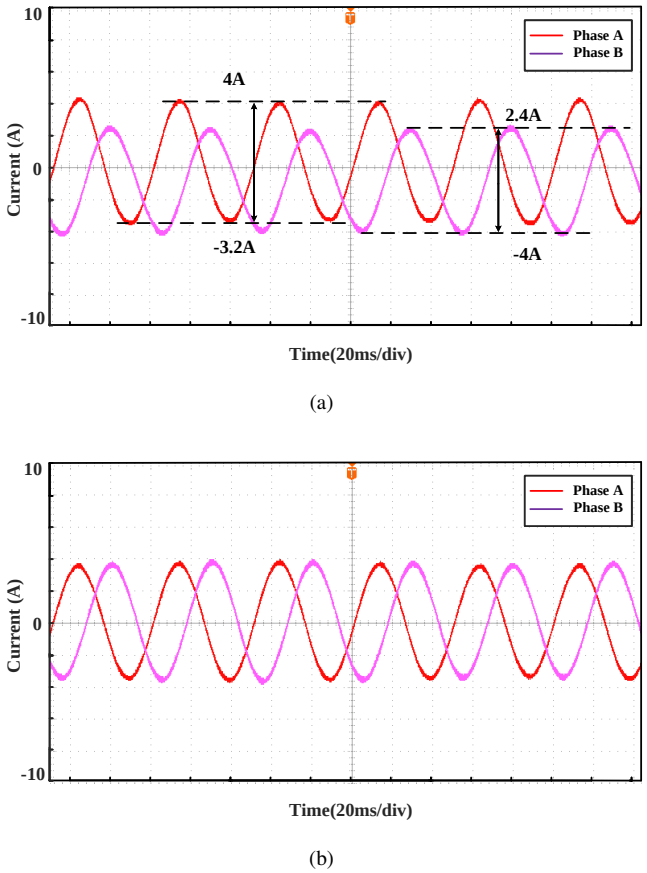

Fig. 8. Comparison of motor phase currents. (a) Without compensation. (b) With compensation.

C. Experiments on Robustness Verification

The proposed CME compensation method does not rely on motor parameters, thus eliminating the impact of parameter mismatch on compensation effectiveness. Although parameter mismatch may affect the performance of current loop decoupling, the proposed method indirectly estimates and applies compensation through an integral controller in a closed loop to achieve convergence. To further demonstrate the parameter

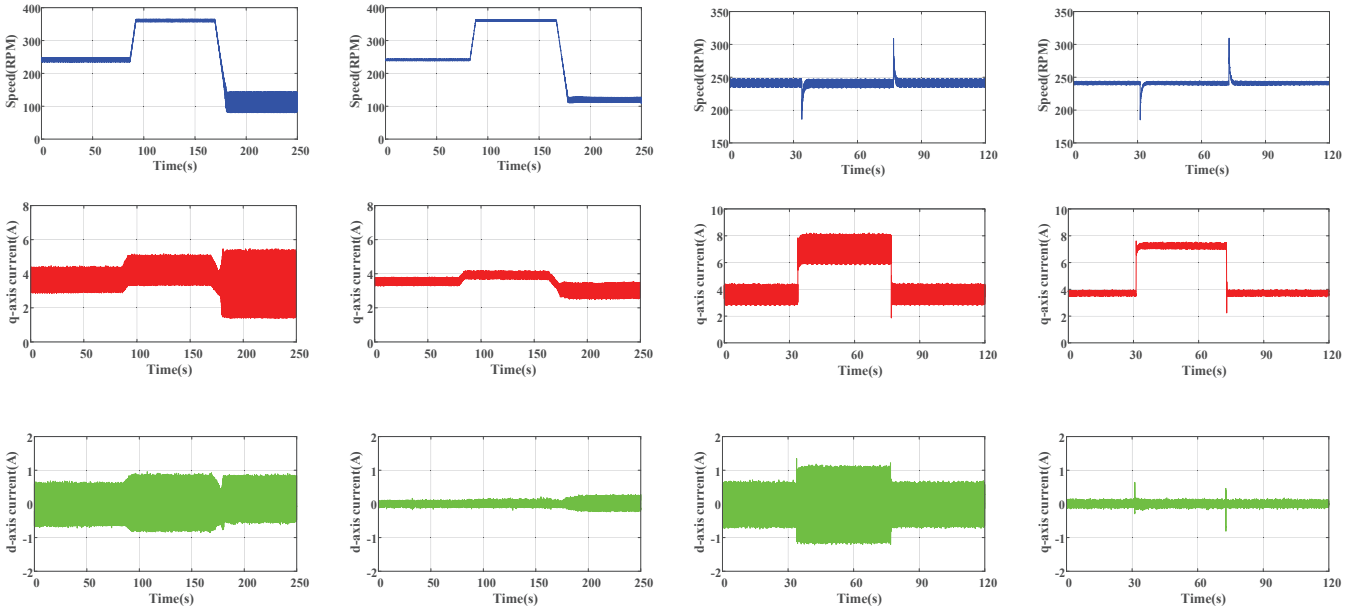

(a) (b) (c) (d)

Fig. 9. Experimental waveforms of speed and *dq*-axis current with and without CME compensation method (a) Speed change processes without compensation. (b) Speed change processes with compensation. (c) Load change processes without compensation. (d) Load change processes with compensation.

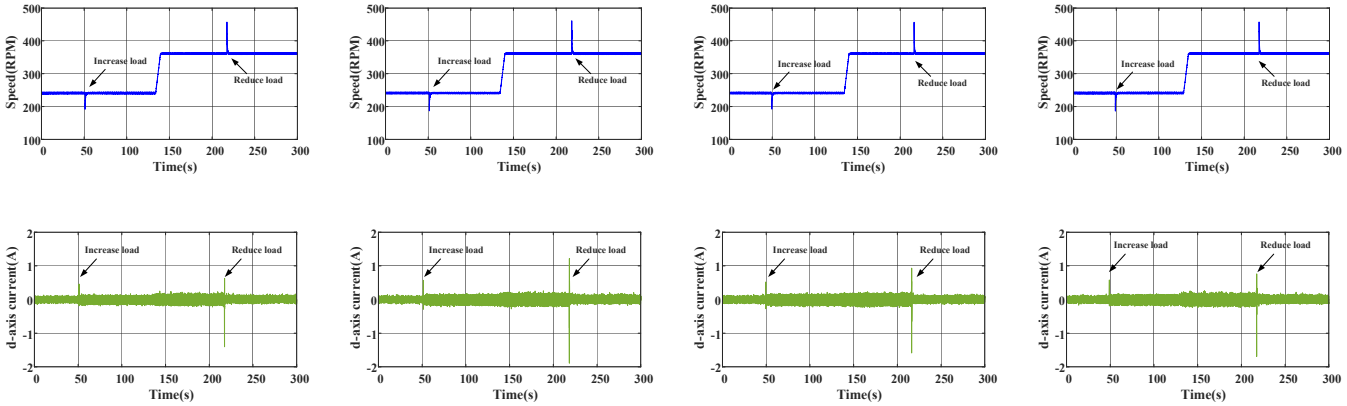

(a) (b) (c) (d)

Fig. 10. Experimental waveforms of speed and *d*-axis current under CME compensation method when speed and load change under motor parameter mismatch. (a) 120% L_s. (b) 80% L_s. (c) 120% R_s. (d) 80% R_s.

robustness of the proposed method, experiments are conducted using mismatched motor parameters, as shown in Fig. 10. The Fig. 10 (a), (b), (c), and (d) show the results when the stator inductance and resistance were respectively set at 120% and 80% of their correct values. As shown in Fig. 9(b), (d) and Fig. 10, the performance remains similar even with different parameter mismatches compared to the scenario with correct parameters.

V. Conclusion

This article presents a compensation method to solve the current measurement errors and the resulting speed ripple problem in motor drive systems. The proposed method focuses on decoupling and compensating for CME by utilizing the current ripple component. By considering the impact of the closed-loop system, the proposed CME compensation method effectively extracts the periodic ripple component in the d-axis current through the incorporation of adaptive band-pass filters. The method significantly reduces ripples in dq-axis currents and speed, while also demonstrating high robustness to motor parameters. The proposed method does not require any additional hardware and can be implemented straightforwardly. Experimental results validate the efficiency and practicality of the proposed CME compensation method.

REFERENCES

[1] J. Chen, X. Yuan, F. Blaabjerg, and C. H. Lee, "Overview of fundamental frequency sensorless algorithms for ac motors: A unified perspective," *IEEE Journal of Emerging and Selected Topics in Power Electronics*, vol. 11, no. 1, pp. 915–931, 2022.

[2] S.-H. Song, J.-W. Choi, and S.-K. Sul, "Current measurements in digitally controlled AC drives," *IEEE Industry Applications Magazine*, vol. 6, pp. 51–62, Jul 2000.

[3] D.-W. Chung and S.-K. Sul, "Analysis and compensation of current measurement error in vector-controlled AC motor drives," *IEEE Transactions on Industry Applications*, vol. 34, pp. 340–345, Mar 1998.

[4] D. Mohanraj, J. Gopalakrishnan, B. Chokkalingam, and L. Mihet-Popa, "Critical aspects of electric motor drive controllers and mitigation of torque ripple-review," *IEEE Access*, pp. 73635–73674, Jan 2022.

[5] S. Suzuki and M. Yoshida, "Elevator control apparatus with compensation for current sensor offset voltage," Apr. 18 1995. US Patent 5,407,027.

[6] M.-S. Kim, D.-H. Park, and W.-J. Lee, "Compensation of current measurement errors due to sensor scale error and non-simultaneous sampling error for three-phase inverter applications," *Journal of Power Electronics*, pp. 31–39, Jan 2022.

[7] M.-S. Yoo, S.-W. Park, H.-J. Lee, and Y.-D. Yoon, "Offline compensation method for current scaling gains in AC motor drive systems with three-phase current sensors," *IEEE Transactions on Industrial Electronics*, vol. 68, no. 6, pp. 4760–4768, 2020.

[8] B. Wang, M. Tian, Y. Yu, Q. Dong, and D. Xu, "Enhanced ADRC with quasi-resonant control for PMSM speed regulation considering aperiodic and periodic disturbances," *IEEE Transactions on Transportation Electrification*, vol. 8, pp. 3568–3577, Sep 2022.

[9] W. Qian, S. Panda, and J.-X. Xu, "Torque ripple minimization in PM synchronous motors using iterative learning control," *IEEE Transactions on Power Electronics*, pp. 272–279, Mar 2004.

[10] M. Tang, A. Formentini, S. A. Odhano, and P. Zanchetta, "Torque ripple reduction of PMSMs using a novel angle-based repetitive observer," *IEEE Transactions on Industrial Electronics*, pp. 2689–2699, Apr 2020.

[11] S. Lee, H. Kim, and K. Lee, "Current measurement offset error compensation in vector-controlled SPMSM drive systems," *IEEE Journal of Emerging and Selected Topics in Power Electronics*, pp. 2619–2628, Apr 2022.

[12] K.-R. Cho and J.-K. Seok, "Correction on current measurement errors for accurate flux estimation of AC drives at low stator frequency," *IEEE Transactions on Industry Applications*, vol. 44, pp. 594–603, Jan 2008.

[13] Y. Zuo, H. Wang, X. Ge, Y. Zuo, A. T. Woldegiorgis, X. Feng, and C. H. T. Lee, "A novel current measurement offset error compensation method based on the adaptive extended state observer for IPMSM drives," *IEEE Transactions on Industrial Electronics*, pp. 3371–3382, Apr 2024.

[14] W.-H. Chen, J. Yang, L. Guo, and S. Li, "Disturbance-observer-based control and related methods—an overview," *IEEE Transactions on industrial electronics*, vol. 63, no. 2, pp. 1083–1095, 2015.

[15] H.-S. Jung, S.-H. Hwang, J.-M. Kim, C.-U. Kim, and C. Choi, "Diminution of current-measurement error for vector-controlled AC motor drives," *IEEE Transactions on Industry Applications*, pp. 1249–1256, Sep 2006.

[16] M. Kim, S.-K. Sul, and J. Lee, "Compensation of current measurement error for current-controlled PMSM drives," in *2012 IEEE Energy Conversion Congress and Exposition (ECCE)*, Sep 2012.

[17] Q. Zhang, H. Guo, Y. Liu, C. Guo, F. Zhang, Z. Zhang, and G. Li, "A novel error-injected solution for compensation of current measurement errors in PMSM drive," *IEEE Transactions on Industrial Electronics*, vol. 70, pp. 4608–4619, May 2023.

[18] G. Hui, B. Chenghao, Z. Hongjun, L. Fanghui, and L. Lei, "Synchronization error estimation of high-speed ad sampling based on digital phase discrimination," in *2018 Cross Strait Quad-Regional Radio Science and Wireless Technology Conference (CSQRWC)*, Jul 2018.

[19] D. Retianza, J. Duivenbode, and H. Huisman, "Plant-independent current sensor gain error compensation for highly dynamic drives," *IEEE Transactions on Industrial Electronics*, vol. 70, pp. 9948–9958, Oct 2023.

[20] T. Estrabis, M. Pelzl, R. Cordero, W. Suemitsu, L. Galotto, and G. Gentil, "Analysis of measurement error compensation of stationary $\alpha\beta$ stator currents done through auto-associative neural network," in *IECON 2021 – 47th Annual Conference of the IEEE Industrial Electronics Society*, Oct 2021.

[21] Y. Zuo, X. Zhang, C. Lai, and L. Iyer, "Correction of current measurement scaling and offset errors for permanent magnet synchronous machine drives," in *2023 12th International Conference on Renewable Energy Research and Applications (ICRERA)*, Aug 2023.

[22] M. Hu, W. Hua, Z. Wu, N. Dai, H. Xiao, and W. Wang, "Compensation of current measurement offset error for permanent magnet synchronous machines," *IEEE Transactions on Power Electronics*, pp. 11119–11128, Oct 2020.

[23] Y. Bai, B. Li, Q. Wang, D. Ding, G. Zhang, G. Wang, and D. Xu, "An adaptive-frequency harmonic suppression strategy based on vector reconstruction for current measurement error of PMSM drives," *IEEE Transactions on Power Electronics*, vol. 38, no. 1, pp. 34–40, 2022.

[24] A. Gholipour, M. Ghanbari, E. Alibeiki, and M. Jannati, "Sensorless foc strategy for current sensor faults in three-phase induction motor drives," *Journal of Operation and Automation in Power Engineering*, vol. 11, no. 1, pp. 1–10, 2023.

[25] H. Zhu and H. Fujimoto, "Suppression of current quantization effects for precise current control of SPMSM using dithering techniques and Kalman filter," *IEEE Transactions on Industrial Informatics*, vol. 10, pp. 1361–1371, May 2014.

[26] F. Briz, M. Degner, and R. Lorenz, "Analysis and de-

sign of current regulators using complex vectors," *IEEE Transactions on Industry Applications*, vol. 36, no. 3, pp. 817–825, 2000.

[27] J. Sorensen and D. O'Sullivan, "A system approach to understanding the impact of non-ideal effects in a motor drive current loop," in *PCIM Europe 2016; International Exhibition and Conference for Power Electronics, Intelligent Motion, Renewable Energy and Energy Management*, pp. 1–8, VDE, 2016.